# Extending Reach Inside the MRI Bore: a 7-DOF, Low-Friction, Hydrostatic Teleoperator

Samuel Frishman, *Student Member, IEEE,* Robert D. Ings, Vipul Sheth, Bruce L. Daniel, *Member, IEEE,* and Mark R. Cutkosky, *Fellow, IEEE*

***Abstract*—We present a hydrostatic teleoperator that provides physicians remote access inside the MRI bore and enables real-time MRI guided interventions such as liver biopsies. The device consists of a custom six-axis arm and a needle insertion end effector. The manipulator is passive and backdrivable with a near one-to-one mapping of motions and forces between the input and output. The six-axis arm translates and orients the needle during insertion and passively reflects respiratory motion while maintaining contact with the skin surface. Arm joints employ novel rotary rolling-diaphragms that provide stiff and low-friction rotational motion without the need for cables, belts, or gear mechanisms found in other solutions. We perform experiments to characterize the device's force and position tracking and demonstrate its functionality with path following tasks. Our results find a system roll-off frequency at 20Hz and that teleoperation tasks are performed comparably to holding the output directly. We motivate the need for force transparency in MRI guided biopsies with a user study in which five radiologists perform phantom membrane puncture biopsies using the needle insertion mechanism. The results indicate a 50% reduction in scans and a 14.5% decrease in membrane overshoot when force feedback is present.**

***Index Terms*—Teleoperation, MRI, force feedback, hydrostatic.**

## I. Introduction

MAGNETIC resonance (MR) offers safe, high contrast imaging of soft tissue inside the body, often superior to ultrasound (US) and computed tomography (CT). Today, MRI is predominantly used for diagnostic and preoperative imaging with limited ability to leverage it for guidance during surgical intervention. Poor access inside the MRI bore prohibits tool manipulation while patients remain inside the machine [1]. In current biopsies conducted with MRI guidance, patients are removed from inside the bore for needle insertion and adjustment. The procedure is conducted step-wise, with incremental needle advancement between imaging scans and the patient repeatedly moved in and out of the bore [2]. We present an MRI compatible teleoperator that provides remote access inside the machine from several meters and enables needle manipulation without the need to remove the patient between imaging scans. The device is passive – all motions and forces originate from the operator and are transmitted to the output via hydrostatic lines. The lines are low-friction and high stiffness, providing transparent reflection of forces and motions at each end. Moreover, backdrivability allows the system to conform to patient respiratory motions and makes possible biopsy of organs in the abdominal cavity, such as the liver.

The device consists of two primary subsystems, depicted in Fig. 1: a six-axis arm for adjusting needle position and angle, and a single-axis insertion mechanism for advancing/retracting the needle. Arm joints utilize novel rotary rolling-diaphragms, recently introduced in [3], which provide rotary actuation without belts, cables, gears or other conversion schemes. At the end of the arm, a curved support beam contacts the body, centered around the point of needle insertion, to further stabilize the needle and facilitate passive tracking of patient respiratory motions. The needle is actuated with a linear mechanism based on precision ground glass cylinders introduced in [4]. This technology affords precise and nearly frictionless transmission of interaction forces from the patient side to the control side.

In the following sections we first review related work on which this new study draws. We then present results of an initial test conducted with physicians using just the final, needle insertion axis of the system. The results of this test, which confirm that a combination of high fidelity force feedback and MRI imaging is superior to either modality alone, motivate the design and testing of the complete arm and needle system, presented in the following sections. We conduct experiments that demonstrate device functionality and MRI compatibility and conclude with discussion of additional design considerations for improving the system.

### A. Related Work

Researchers have investigated devices to enable in-bore MRI-guided biopsies for over a decade [5], leveraging a number of technologies to satisfy MRI compatibility requirements. Notably, two directions have been explored: pneumatic and piezoelectric systems. Prominent examples of pneumatically powered robots include those from Stionaovici et al. [6] and Soteria Medical [7]. These systems, and most other MRI compatible robots [8]–[11], are designed for prostate biopsy. The position of the prostate and approach direction of the needle allow the devices to encompass a relatively large volume inside the MRI bore with only the patient's legs as obstacles. For other organs, such as the liver and pancreas, needle insertion occurs between the patient's torso and bore wall, imposing severe space constraints. Groenhuis et al. present a pneumatic stepper motor, similar to [6] and [7], in a compact form factor

S. Frishman and M.R. Cutkosky are with the Department of Mechanical Engineering at Stanford University, Stanford, CA, 94305 USA

R.D. Ings is with Mirsee Robotics, Cambridge, ON N1S 2L9, Canada

V. Sheth and B.L. Daniel are with the Department of Radiology at Stanford University, Stanford, CA, 94305 USA

Contact author: samuel9@stanford.edu

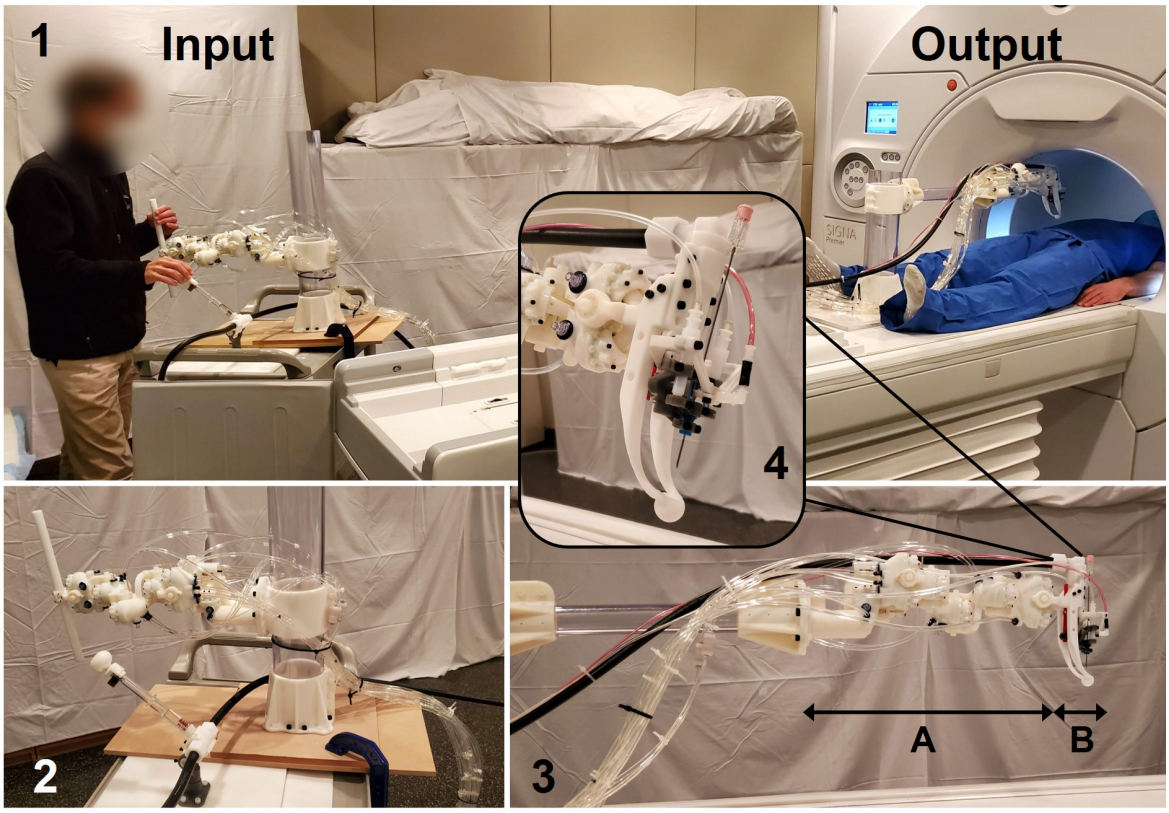


Fig. 1: (1) The teleoperation system for in-bore access. A physician manipulates the input and directly controls position and orientation of the needle inside the bore. (2) A view of the operator side. The two inputs provide independent control of needle insertion and needle position/angle adjustment. (3) The output arm (A) and needle insertion mechanism (B). The arm enables orienting and translating the needle while the insertion mechanism is used for inserting the needle. (4) A closeup of the insertion mechanism. The spherical end rests on the patient's skin at the puncture location.

for in-bore breast biopsies [12]. Such devices however, are not backdrivable. For prostate and breast, respiration has little impact on organ position, but this is not true for organs such as the liver. In [13], Franco et al. present a five degree-of-freedom (DoF) MRI-compatible, pneumatically actuated robot for liver ablation but discuss challenges due to respiration.

Robots with piezoelectric motors have also been explored [14], [15]. These devices can be constructed from non-ferrous materials and, because they use a low current, can be made compatible with MRI applications. However, they do employ some metallic components and affect imaging signal to noise ratio [15], [16] or require specialized sequences and integration with scanner software. Moreover, they are inherently admittance systems, stiff and not backdrivable, so they cannot accommodate patient motion without active closed-loop control.

Whether pneumatic or piezoelectric, the systems described above are active: energy is introduced into the system, with attendant safety and stability concerns. In addition, unless equipped with a powered haptic interface on the physician side, they relegate the perception of interaction forces to visual displays. Force feedback has been recognized as beneficial in cases where vision is limited [17], and we discuss the role of force feedback in MRI-guided interventions in section I-B.

As noted earlier, our system utilizes hydrostatic rolling-diaphragm technology. Hydrostatic systems provide power-dense actuation and ease of routing as compared to cables or belts. Traditional hydraulics, however, rely on sliding seals that introduce significant stick-slip friction. Rolling-diaphragm transmissions have been explored for short distance telemanipulation applications such supernumerary limbs [18], telepresence robots [19], and grippers [20]. Recently, such transmissions have also been applied to medical systems [21]–[24] including our own work on a single axis needle insertion device [4], [25]. Rolling-diaphragms provide a dynamic seal that is stiff and has very low Coulomb friction. They enable transmissions that exhibit a desirable combination of power density and impedance rendering ability, superior over long distances to linkages, belts, or cables. Though long-stroke rolling-diaphragms have been explored [26], [27], commercially available versions are limited to a stroke-to-diameter ratio of roughly one, creating a trade-off between form factor and actuator range of motion. Moreover, multi-axis robotic systems often favor rotary joints in serial chain for a large workspace, requiring belts, capstans, or gears to convert motion at each joint. The work in this paper builds upon recently developed rotary rolling-diaphragm actuators, introduced in [3]. To our knowledge it is the first application of this technology.

### B. Effect of force feedback in MRI-guided biopsy

Before fabricating and testing the entire arm and needle insertion system we conducted an initial study with interventional radiologists of just the needle insertion subsystem to explore the benefits of combined imaging and force reflection. The role of haptic feedback in surgical robotics varies greatly between different procedures. In percutaneous biopsies, interventional radiologists often report leveraging tactile cues for guidance in needle insertion. Physicians discuss feeling the needle transition between tissue types, puncture through membranes, or entering a mass. Despite such anecdotal support, and though explored in other domains (e.g. ultrasound [28] or robot-assisted insertion more generally [29]), the benefits of haptic feedback in MRI-guided biopsies remain unquantified. Previous studies on needle insertion tasks have found visual feedback to dominate and force feedback to be most relevant in cases where vision is limited [17], as is often the case in MRI. While MRI provides superior soft tissue contrast compared to CT or US, images are of relatively low-resolution compared to standard RGB cameras. Slow acquisition rates (often several seconds per scan) and needle artifact (commonly over 5 mm in diameter [30], [31]) further inhibit scan quality. To better understand the role of force feedback in MRI-guided biopsy and motivate a force transparent system, we conducted a study (IRB-26526) that evaluates physicians performing in-bore MRI-guided biopsies in phantom tissue with and without force feedback (Fig. 2). The study enrolled five radiologists with an average of 7 years practicing.

In the study, physicians inserted a needle into a custom tissue phantom designed to mimic a liver biopsy. The phantom includes a silicone membrane, embedded at a 5.5cm depth, that requires a 1.5N force to puncture with the gauge 18 bevel-tip needle used in the study. Details on the phantom's properties and composition can be found in our previous work [4]. Needle insertion was performed using the final insertion axis of our teleoperation system. Physicians controlled the needle position from a distance by manipulating the input piston of the glass cylinder transmission. Physicians stood outside the 5 Gauss line behind the MRI bed's edge and had a clear view to a computer screen inside the adjacent control room. A study assistant inside the control room would initiate an MRI scan when signaled by the physician who could then view the scan on the computer screen through the window. Scans were single shot fast spin echo with a four second acquisition time. Scan plane alignment to the needle was performed at the beginning of each trial. Two conditions were tested, one with force feedback and one without. In the case with force feedback, physicians controlled the input side of the transmission and perceived forces occurring at the needle through the inherent transparency of the single-axis device. The details and characterization of the glass cylinder transmission are provided in [4]. Briefly, it provides a nearly frictionless motion with force tracking having $\leq 5\%$ input/output discrepancy and a bandwidth of 100 Hz. In the case without force feedback the physicians manipulated a mechanically isolated glass piston attached to a linear encoder (US Digital 2000 LPI Quadrature) that controlled the position of a single-axis stage which, in turn, was connected via a hydrostatic transmission to the needle insertion axis inside the bore. The encoder and motor resulted in a closed loop tracking error of $< 0.05mm$. Thus, with this system physicians could control the needle position precisely but received no reflected force feedback.

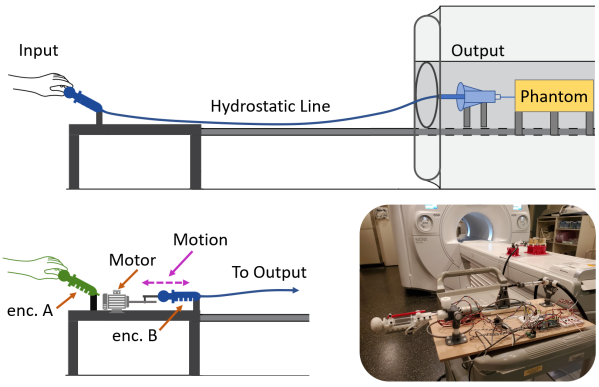


Fig. 2: An illustration of the participant study comparing MRI-guided biopsy under two conditions: (top) with force feedback and (bottom) without. In the case with force feedback (top), the hydrostatic transmission is manipulated directly and forces propagate through the system. In the control case (bottom), the hydrostatic transmission is isolated from the user input. A motorized stage tracks the user input via position encoders and drives the needle. In this case, the participant relies solely on MRI scans as no haptic feedback is present. An image of the motorized system is shown in the bottom right.

Four trials for each case were conducted for a total of 8 recorded insertions per participant. Each trial began with an MRI scan of the needle slightly inserted into the phantom with some variation in distance to reduce a user's ability to memorize the amount of needle advancement between trials. The physician would insert the needle to a desired depth and could request a new MRI scan at any time to view the current position of the needle inside the phantom. The goal of the insertion was to puncture the membrane with minimal overshoot (distance of the needle tip beyond the membrane plane). The number of scans acquired and membrane overshoot were recorded for each trial. Overshoot was calculated using a camera image, taken after the trial with the phantom removed from inside the bore, and pixel ratios based on known markings on the needle (note that the phantom is transparent). This method was used in our previous studies [4] and is accurate to 0.1 mm.

*1) Initial Study Results:* Figure 3 presents sample insertion progressions for both the motorized (A) and direct manipulation cases (B) as well as overall study results. We find that the presence of force feedback halves the number of scans performed and reduces membrane overshoot by 14.5% ($\approx 1mm$) with statistical significance ($p < 0.05$). Moreover, in the motorized case, five false positives occurred as compared to zero in the passive case with force reflection. In these trials, the physicians indicated that they had punctured the membrane based on the MRI scan, however, the membrane

had not been punctured but was deflected. A scan of one such instance is shown in the inset of Fig. 3C. As seen, due to needle artifact and slight needle bending out of plane, it can be challenging to identify puncture vs significant membrane deflection from the scan alone. The drop in force occurring during the puncture event, however, is reliably perceived by touch. We see from the scan progressions that without force feedback, many scans are required as the needle traverses the membrane plane to capture the moment puncture occurs. In the case with force feedback, physicians used the imaging to approach the membrane and then force feedback to identify the puncture moment. We also note that in our previous study without MRI guidance, participants experienced both missed and false positive detections when no vision was provided (i.e. the phantom was obscured) [4]. This occurred even when the task was performed with the needle held directly in hand, indicating that force feedback alone is insufficient to reliably identify the membrane puncture event and further suggests that physicians leveraged both the MRI scans and force feedback to achieve a 100% detection rate in the passive teleoperation case. These results motivate the combined positioning arm and insertion system described in the next section.

## II. Teleoperator Design

Practical constraints have limited clinical translation of devices investigated for in-bore MRI-guided biopsies. To improve clinical applicability, we propose that an ideal teleoperator should have the following properties:

- **Passive:** All force and motions originate from the operator with no added energy. Passivity significantly reduces safety concerns and reduces regulation barriers.
- **Backdrivable:** Backdrivability is important for both force transparency and conformation to respiratory motions, a key element when targeting organs in the torso.
- **Bilaterally Force Transparent:** Accurate force feedback provides intuitive control of the needle, reduces procedure duration, and provides a complimentary sensing modality to the MRI scans. Moreover, transparency in the forward direction (input to output) enables the operator to apply appropriate forces on the tissue.
- **Versatile:** While each organ possesses unique challenges, an in-bore MRI-guided biopsy approach is applicable to half a dozen organs. A device capable of performing a several procedures significantly increases likelihood of commercial translation.

Our solution consists of a six DoF serial chain (arm) that manipulates a single DoF needle insertion mechanism. A serial chain is selected as it provides a large workspace and can be configured to target a number of organs. As a preliminary application, we focus on the liver. Liver biopsy is a convincing initial use case for MRI-guidance because available contrasts enable clear visualization of hepatic tissue for many minutes (30min) as compared to a few dozen seconds with CT. Moreover, MRI provides higher sensitivity of lesions than US or CT [32] and certain lesions are only visible with MRI. With minor modification, the arm design presented in this work is suitable for additional organ biopsies including the prostate, breast, pancreas, and thyroid.

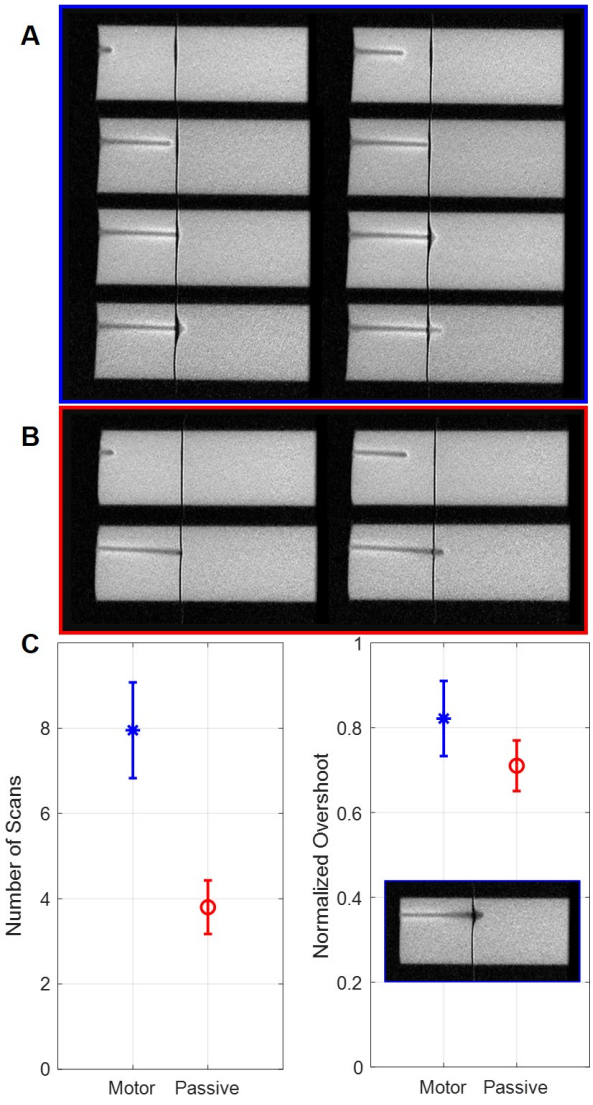


Fig. 3: Evaluating the benefit of force feedback in MRI-guided membrane puncture. (A) A sample scan progression without force feedback. (B) A sample scan progression with force feedback. (C) Final results from a user study with five Radiologists; a significant decrease in scans utilized and membrane overshoot is observed.

### A. Six-Axis Arm

Figure 4A illustrates the six-axis kinematic chain with link lengths presented in Table I as Denavit Hartenberg (DH) parameters [33]. The dimensions are motivated by a workspace analysis, presented below, and practical constraints arising from actuator size and tube fittings. The axis order and configuration are designed to accommodate a low profile – an initial height less than the length of a 15 cm needle – and to reduce distance between joints two and six. An initial horizontal roll joint was placed at the base. While this choice results in the first axis rotating the majority of the arm's mass, it allows us to reduce the maximum moment experienced at the second joint as compared to making the final axis a roll joint, as is common in industrial robots. Even so, for available

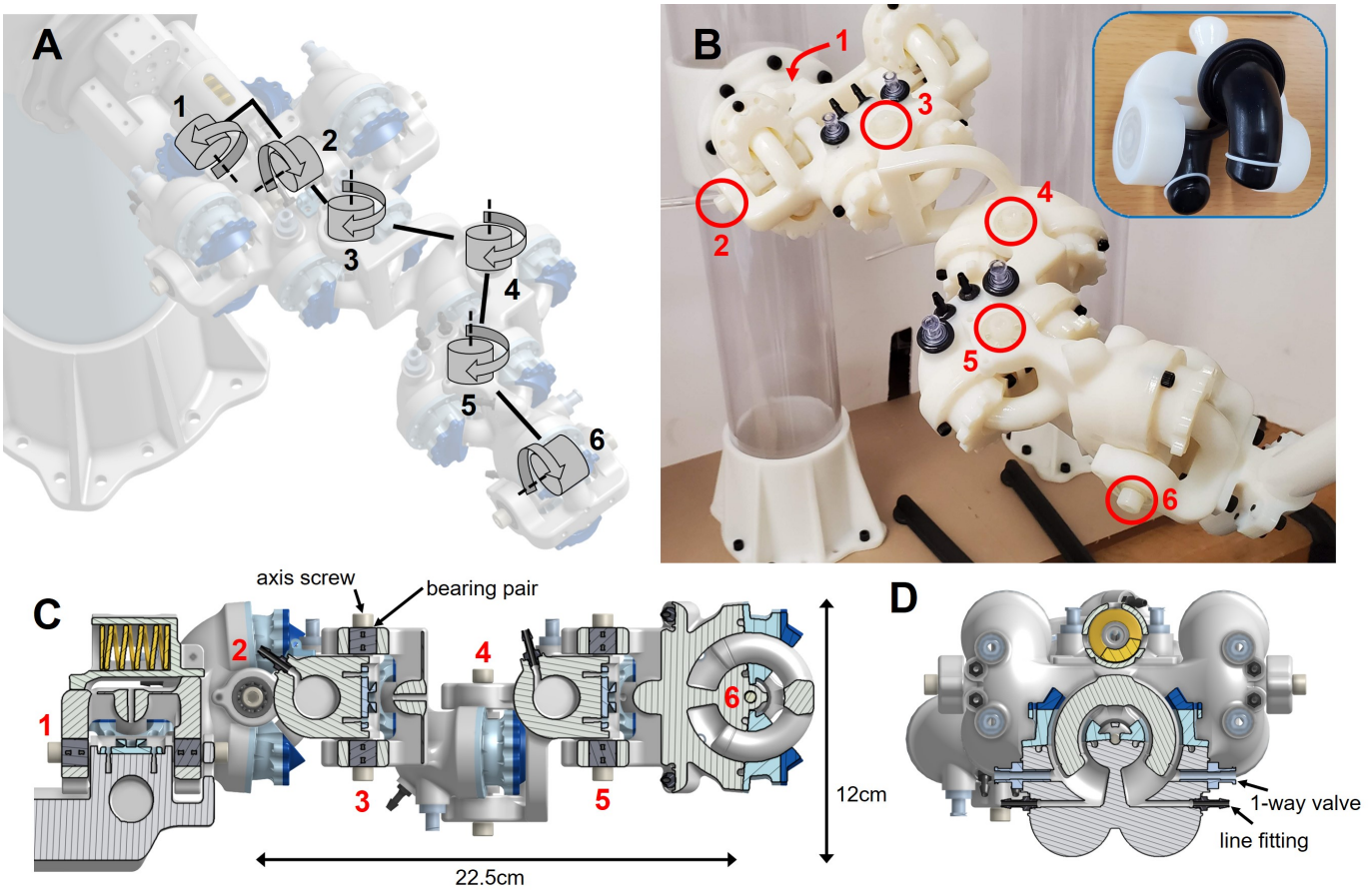


Fig. 4: (A) An illustration of the arm kinematics. (B) The arm prototype with associated joint axes labeled. Inset shows toroidal pistons with mounted rotary rolling-diaphragms. (C) A cross-section view of the arm illustrating the fluid chambers and toroidal pistons. (D) A cross-section view depicting the filling system for each fluid chamber.

diaphragm dimensions (20 mm piston diameter and 22.5 mm arc radius) and an arm length of ≈30 cm, a 20 N force (the maximum force expected during soft-tissue biopsy) results in nearly 700 kPa pressure in joint two. When added to the baseline operating pressure of the system, this approaches the rated limit of many off-the-shelf plastic fittings and tubing. To halve this pressure, the second joint includes a second actuator operating in parallel.

Filling lines with fluid and removing all air is a challenge in hydrostatic systems. To reduce trapped air, each chamber includes a filling and exit port (Fig. 4D), allowing fluid to cycle through the system during the filling process. The filling ports house an MRI-safe one-way valve (Inject Tech CV0006), providing a compact method for creating a self-closing inlet. The one-way valves also act as a mechanical safety, limiting the torque each joint can apply; if pressure exceeds the maximum back pressure rating (2 MPa) fluid bleeds through the one-way valve. At the end of the filling process, the lines were pressurized to 450 kPa. Pressure was adjusted at the beginning of each day of testing, however, with improved tolerancing and part surface finish, rolling-diaphragm seals are capable of forming a leak free system.

Each joint of the input and output arms is identical, with tubing connecting the respective joint chambers. Fluid lines are crossed, to achieve a one-to-one mapping of motion; a clockwise rotation at the input results in a clockwise rotation at the output. Actuation is transmitted with toroidal piston pairs, sealed by rotary rolling-diaphragms. Opposing piston pairs enable operating the system at a nominal pressure (450 kPa), which is necessary to maintain a convolution in the rolling-diaphragms. The initial internal pressure also limits the maximum pull or withdrawl force, as a negative pressure would produce cavitation and diaphragm inversion [19].

| $J$ | $d$ | $\theta$ | $r$ | $\alpha$ |
|---|---|---|---|---|
| 1 | 5.5 | 0 | 2.5 | 90 |
| 2 | 0 | 90 | 5 | 90 |
| 3 | -2.5 | 44.2 | 7.6 | 0 |
| 4 | 2.5 | -88.4 | 7.6 | 0 |
| 5 | 0 | 44.2 | 6.7 | 90 |
| 6 | 0 | 0 | 5 | 90 |

TABLE I: DH parameters for the constructed arm prototype. Link lengths are motivated by a workspace optimization (Fig. 5) and practical constraints from available fittings, fasteners, and rolling-diaphragms.

*1) Counterbalancing:* An ideal manipulator for transparent teleoperation includes gravitational force compensation. In our design, joint 2 is the axis most affected by the arm's weight and is compensated using a plastic spring fixed to the first

joint (see Fig. 4C). A Dyneema line is attached to the end of the spring and anchored on joint 2. As joint 2 rotates downward, the spring is compressed. This compensation results in a design with the arm biased toward its neutral position (determined by the spring preload). An item for future work is to replace this spring with a plastic pneumatic cylinder, to provide counterbalancing with nearly constant force.

*2) Workspace:* Workspace requirements vary by organ and typical parameters for liver biopsy can be found in [1], [13]. In this prototype, arm dimensions are chosen based on a workspace analysis aimed at maximizing available motion at the skin incision region. We assume that the center of the device's workspace is aligned near the incision point prior to the intervention and telemanipulation is primarily used for adjustments made after the needle has punctured the skin. Translation in this region is limited by skin stretch and therefore the range of possible needle angles is a primary optimization metric. Specifically, we consider the range of orientations the arm can achieve at a set of points within a 2 cm radius of the incision (beyond this radius a physician would typically retract and re-insert the needle at a new incision point). We conduct the optimization in MATLAB using the Robotics Toolbox and a genetic algorithm. The cost function is defined as the the summation of reachable volumes at points within a 2 cm radius. Volumes are computed by evaluating the range of angles through which the arm can orient the needle when pivoting about a given point in the set. The pivot point and reachable points just below the skin surface form a convex hull (Fig. 5 C). The summation of the hulls for each point in the set defines the overall post-incision reachable volume. While the GA includes bounds for each link, maximizing workspace alone does not consider device footprint or resulting arm length. Arm length significantly impacts stiffness and maximum end effector forces. To better inform the design, we perform an additional multi-objective optimization that maximizes the workspace metric described above while minimizing the arm length. The results are show in Fig. 5 D & E, and show that increasing workspace alone results in a significant growth in overall arm length. The multi-objective optimization, however, elucidates link length combinations that both increase the workspace while reducing arm length. The selected dimensions for the prototype are listed in Table I as DH parameters.

*3) Transmission:* Tubing choice plays a role in transmission stiffness. In this prototype, 1/4inch (6.4mm) outer diameter, 1/8inch (3.2mm) inner diameter polyurethane tubing was employed in the arm (McMaster #5648K74) for its favorable combination of maximum working pressure (1.8MPa), minimum bend radius (13mm), visual transparency, and low-cost. While maximum pressure depends on a number of factors (e.g. diameter and wall thickness), for given tube dimensions, a larger pressure rating corresponds to a stiffer line. Clear tubing of stiffer material (FEP, McMaster #2129T16) was considered, however, it is categorized as semi-flexible and results in significant resistance to arm motion when bent. Some tube bending is expected as routing all lines centrally through joint rotation axes is impractical. Hydraulic swivel fittings can reduce tubing resistance to motion, however, standard swivel fittings include metal components or require a large footprint. Fabric reinforced tubing offers additional stiffness and can exhibit significant flexibility, however, clear tubing was desired to enable visual inspection during the filling process to ensure absence of air in the transmission. In this prototype, we struck a balance between tube flexibility and stiffness; the polyurethane tubing was used in the arm itself and FEP tubing (max pressure 3 MPa) was used in the long runs between the arms. We note that in this application, where maximum expected input forces are 20 N and transmission length is three meters, line compliance due to hoop expansion of tubing is sub 0.03 mm for tubing of Young's moduli in the range of 20-100kPa. Tubing compliance calculations can be found in [4], [34]. Tubing elasticity represents a relatively small contribution to overall system compliance.

### *B. Insertion End Effector*

A needle insertion mechanism (Fig. 6) mounts to the end of the six-axis arm and uses a pneumatic clutch for grip and release of the needle. The insertion mechanism is controlled via the glass cylinder transmission described in the participant study and first introduced in our previous work [4]. The clutch mechanism, also introduced in [4], enables a compact design with actuation parallel to the needle and an initial configuration similar to needle's length. This is critical for fitting the device in the space between the patient and bore wall, which is often constrained to less than 20 cm. The needle is advanced through multiple short strokes, analogous to driving a needle directly in hand. The needle is gripped near the tip, inserted part way, re-gripped further up, and inserted deeper. Grip and release are achieved with a collet and controlled by the operator via a foot-pedal valve. The operator manipulates the needle's insertion depth, and position of re-grip, via the glass cylinder transmission.

The insertion mechanism includes a protruding curved beam that is initially positioned at the entry point on the skin. The beam is fixed to the sixth joint of the arm and transmits forces from the body wall directly to the arm, rather than through the needle, and vice versa. This enables patient respiration to be reflected in the system and allows maintaining contact with the body wall while driving the needle. The distance the beam protrudes beyond the needle driver defines the maximum length of a single insertion stroke (red arrow in Fig. 6). In this prototype, 3.5 cm was selected as a balance between overall length of the mechanism and insertion stroke. We note that the beam is easily detachable and, like the needle, is considered a disposable and replaced after each procedure.

## III. Evaluation

Tests were conducted to evaluate the system's transparency and ability to follow respiratory motions. Functional testing also investigated an operator's ability to use the device in telemanipulation tasks and compared the results to direct manipulation. Additionally, though the device is constructed entirely of non-conductive materials, an MRI compatibility test was performed to ensure minimal impact on imaging SNR.

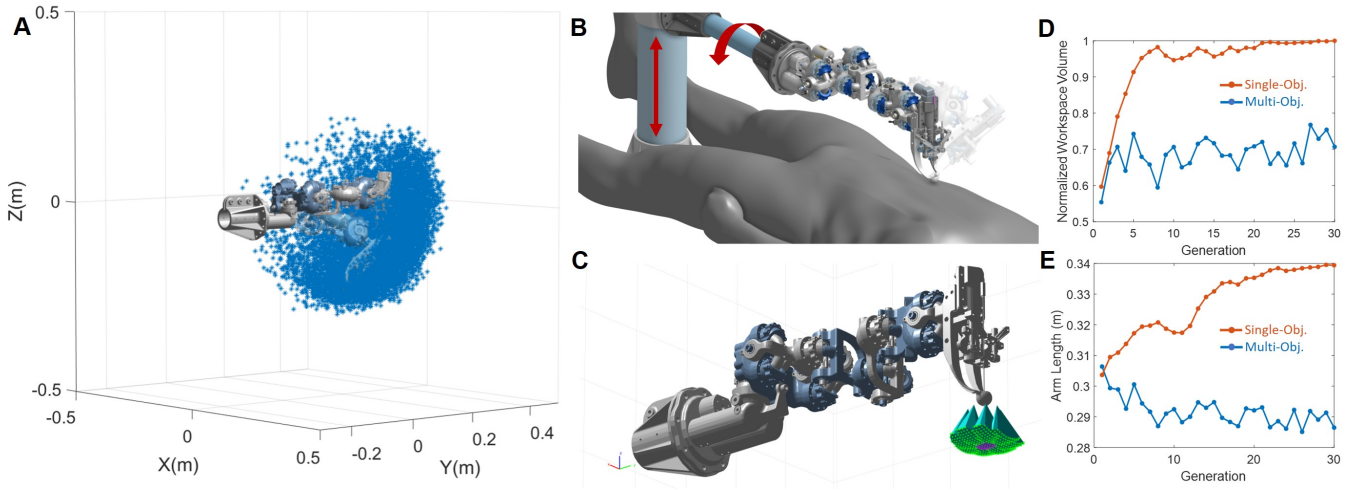


Fig. 5: (A) The arm's reachable workspace depicted by 10000 points. (B) The fixed adjustment degrees of freedom. Prior to the procedure, the arm's height and angle can be varied depending on patient size and puncture point. (C) The convex hulls depicting the maximum angling of the needle at given locations. (D) Optimizing arm link lengths to maximize procedural workspace and (E) arm length. The single objective function only considers workspace while the multi-objective additionally minimizes arm length.

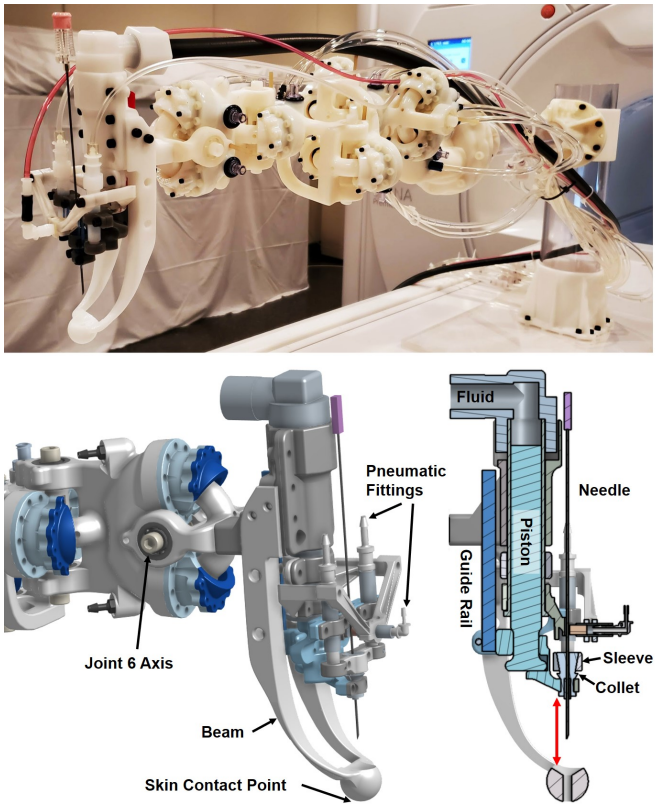


Fig. 6: The insertion mechanism mounted to the arm. The mechanism includes a curved beam which makes contact with the skin surface and transmits body wall force to and from the arm. The needle traverses through the endpoint and is controlled with a custom, glass cylinder transmission and clutch presented in our previous work [4].

### A. *System Transparency*

System transparency determines a teleoperator's ability to remotely perceive forces occurring at the needle. System stiffness also influences an operator's control of the output position. We investigate position and force tracking using a camera system and force sensors mounted at the input and output.

*1) Position Tracking:* Reflective markers were mounted on rods attached to the sixth joint of the input and output arms and the input was manipulated in free space. Six overhead cameras (OptiTrack, calibration x y z) tracked the position of each arm at 60fps. Data were gathered for a sample trajectory and for cases with each joint isolated.

*2) Force Tracking:* Force transparency was evaluated along the axis perpendicular to the arm – the axis most critical for reflecting needle forces and respiratory motions. A system identification was performed by mounting force sensors (Futek FSH00103) at each end of the device and oscillating the input with the output fixed against a hard stop. An up-chirp force was applied by a muscle lever (Cambridge Tech., Model 6900) of amplitude 1.25 N and swept frequencies from 0.15 to 150 Hz. Force sensor data were acquired at 500 Hz with an Arduino Due.

In addition to system identification, force impulses were applied and the subsequent device response was recorded. Data were gathered under two different conditions. In the first, the output is fixed and impulses are applied at the input. Forces are recorded at both ends of the system. In the second, both ends are free floating, and an impulse is applied at the output side. The impulse magnitude and position data of both ends are recorded to evaluate the system's ability to reflect small oscillations. Position data were recorded with the overhead camera system.

Lastly, a force sensing probe was attached to the rod at the output arm. A volunteer laid below the arm with the

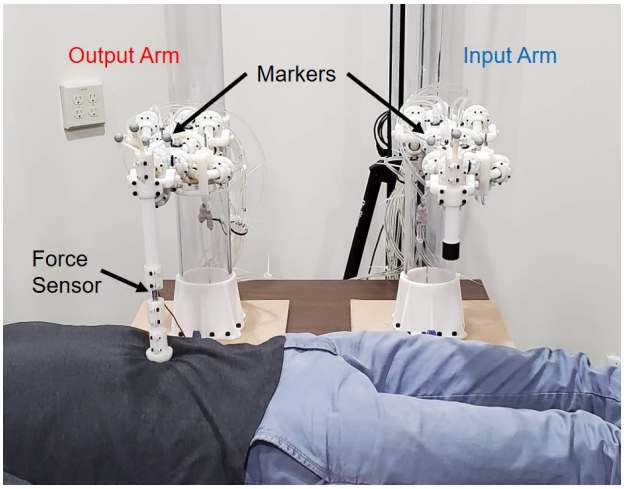


Fig. 7: An experimental setup for capturing the system's ability to reflect respiratory motions. A volunteer lays below the output arm and overhead cameras track the position of markers mounted on the arms. A force sensor captures the associated forces induced from respiration.

sensing probe placed on the their abdomen (Fig. 7). Forces and motions induced in the arms from respiration were recorded.

### B. Path Following

System tracking tests offer valuable insight and predictive power on device capabilities. Ultimately, however, device performance is determined by how well an operator can perform telemanipulation tasks. Functional testing involved using the device to manipulate an ultra-fine tip Sharpie marker along a spherical surface. The surface included a target trajectory consisting of a center circle and four equally spaced lines along the sphere surface (Fig. 8). The circle diameter is 1 cm and line arc lengths are 2 cm, motivated by expected adjustments in a biopsy procedure post insertion. The path is denoted with raised boundaries, sufficiently far apart to avoid any contact with the sharpie. The goal was to draw along the centerline between the walls; error was determined by measuring perpendicular distance from the walls at discrete points along the path. The task was conducted by a single user performing six traces, three via the teleoperator and three manipulating the output directly.

### C. MRI Compatibility

MRI compatibility testing was performed to ensure no observable impact on scan quality from the presence of the device. A GE phantom was placed inside the bore and a single shot fast spin echo (SSFSE) scan sequence was performed with and without the device.

## IV. Results

### A. System Transparency

Figure 9 presents position tracking data for each individual joint isolated (A) as well as a sample trajectory manipulating the full arm system (B). Error in each case is computed as

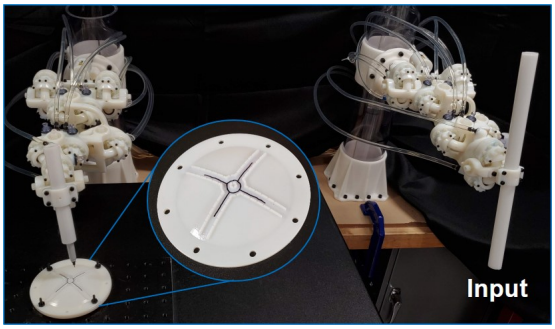


Fig. 8: An experimental setup in which an operator traces a profile using the teleoperator. A control case with the output manipulated directly is also recorded.

the difference in vector magnitudes between input and output positions. Individual joint error is smallest for the base roll joint (J1) and largest for joint 2 with decreasing error for subsequent joints. Motion is tracked at the arm tip and thus joints closer to the base produce larger displacements (with the exception of the base roll joint). Moreover, joint 2 is most affected by the weight of the arm and the spring counterbalance mechanism. Average error for the sample trajectory shown (B) is 4 mm in magnitude and maximum error is 16 mm, though we note that the system tracks even sub-millimeter changes in trajectory profile, an important consideration as human-in-the-loop control enables compensation for a slight offset.

Force tracking data are shown in Fig. 10. Subfigure A presents a bode plot of the frequency sweep applied by the muscle lever. Transfer function estimates are computed using etfe and tfest functions in MATLAB. A resonant frequency is visible near 9 Hz and corresponds to the primary resonant mode of the arm structure. Roll-off begins near 20 Hz and is followed by a second resonant mode near 50 Hz. Figure 10B shows force tracking data for impulses applied to the input with the output fixed. Subfigure C presents position data and associated impulse magnitudes.

Forces induced by respiration and associated motions are presented in Fig. 11. A nominal 2 N force is present at the neutral position and increases roughly 5N during the respiratory cycle. The torso displaces 1.25cm and the remote input reflects this motion with peak error of 0.25 cm and mean error magnitude of 0.14 cm.

### B. Path Following

Results from the path following test are presented in Fig. 12. No statistically significant difference between the teleoperation vs. direct manipulation is found. The data are split into two components: error along the straight sections of the path and error along the central circle. In both cases average error is roughly 0.3 mm with a slight increase in error and variation along the circular trajectory. This is expected as drawing a circle is more challenging than a line.

### C. MRI Compatibility

MRI compatability tests found negligible change in scan SNR in the presence of the device (0.7% change). Fig. 13

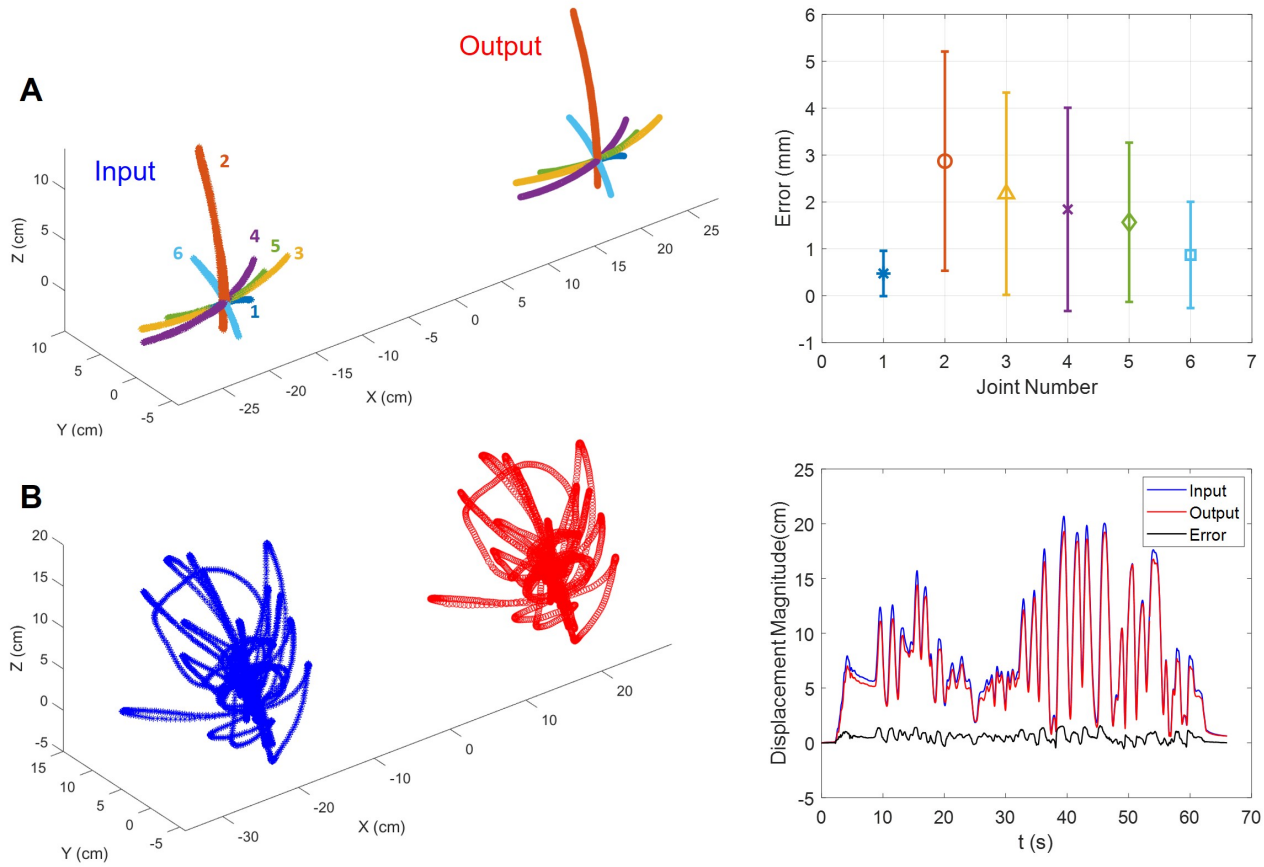


Fig. 9: Position tracking data gather gathered using a camera system. (A) Tracking motion of an individual joint with others fixed. (B) A sample trajectory manipulating the full system.

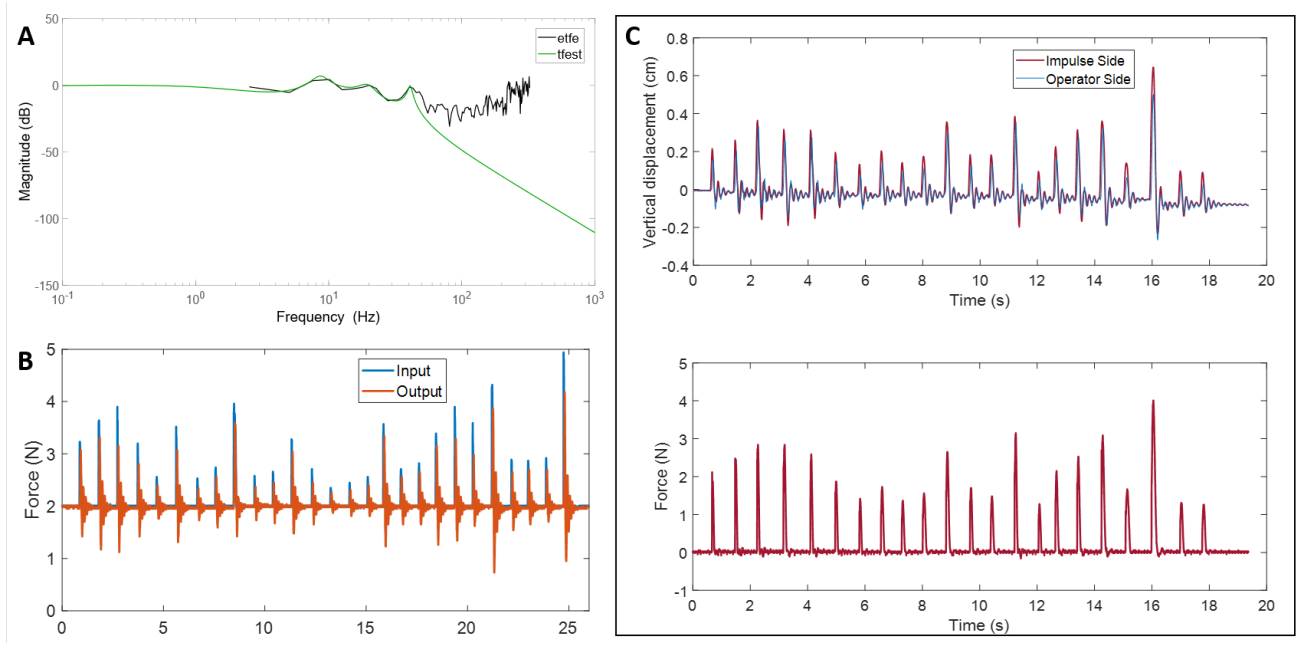


Fig. 10: (A) A bode magnitude plot for system force tracking in the vertical axis. A muscle lever applied an up-chirp signal sweeping frequencies between 0.15 and 150 Hz and sensors mounted at the input and output gathered force data. (B) Force impulses applied at the input with the output fixed. (C) Displacement data for associated force impulses (bottom).

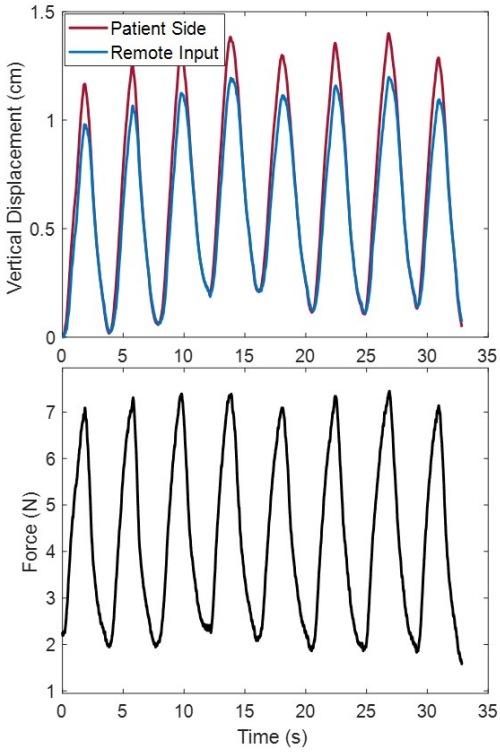


Fig. 11: Data collected during patient respiration. Position tracking finds similar displacements occurring at the remote side, indicating successful reflection of respiratory motion. Associated forces are relatively small, displaying the backdrivability of the system. Forces occur primarily from the weight of the arm, which grows as the arm displaces from the neutral position defined by the counterbalancing spring.

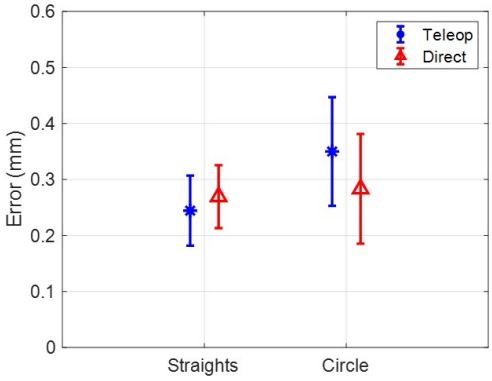


Fig. 12: Results from the path following task. Error from the centerline is shown and is computed separately for the straight and circular sections. No statistically significant difference is found between performing the task via the teleoperator vs direct manipulation.

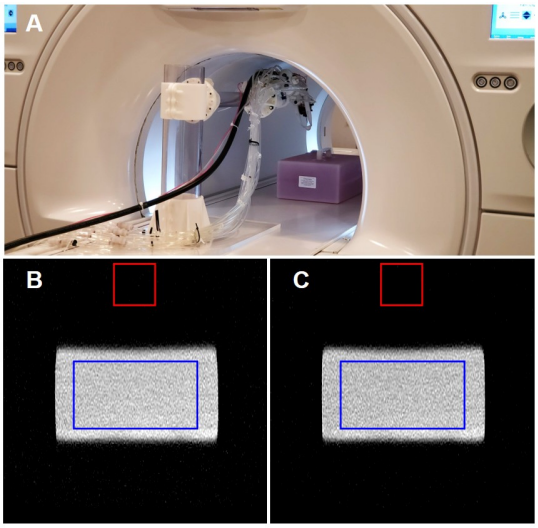


Fig. 13: MRI compatibility testing. (A) The device inside the bore with the phantom. (B) An associated scan of the phantom without the device present and (C) with the device present. The signal and noise regions are depicted and negligible difference in SNR is observed in the presence of the device.

shows the device with the phantom and associated scans with and without the device. Additionally, the signal region and background region are denoted.

## V. Discussion

Our findings demonstrate the system's ability to enable dexterous manipulation inside the MRI bore from several meters. The frequency analysis shows a transmission roll-off near 20 Hz. This is comparable to other hydrostatic devices of this scale [35] and is sufficient for human-initiated motion which is limited to under 10 Hz [36]. We note that for the intended application, motions will be significantly below this physical limit. A structural resonant peak is visible near 10 Hz, corresponding to the primary resonant mode of the arm considered as a fixed beam. We confirmed the natural frequency through a finite element analysis in SolidWorks, which identifies the primary mode at 10.15Hz and secondary mode at 56.28Hz, which is also visible on the bode plot. In the analysis, arm links are combined into a single part and modeled as ABS plastic. The resonant mode may be increased by reducing component mass and increasing the stiffness of each link. Mass reduction additionally reduces inertial forces experienced by the operator, though movements are performed slowly in biopsies. Arm links were 3D printed on an Objet24 out of VeroWhite material (E = 3 GPa). Alternative printers with materials of significantly increased Young's moduli may be used in the future (e.g. Formlabs Rigid with E = 10 GPa). Joint axes consist of M6 glass-reinforced nylon screws (McMaster #97695A116). Larger diameters or brass screws may be used in subsequent designs to improve stiffness of each axis. Additionally, ceramic bearings can replace the low-cost, plastic bearings used in this initial prototype.

While stiffer components may be used to improve transparency, even in this initial prototype, force transients prop-

agate through the system with little distortion as seen in Fig. 10B&C. Impulses as low as 0.25 N are transmitted (B) and sub-millimeter oscillations are reflected (C). Error in absolute position, however, is larger than that observed by typical robotic devices which utilize high resolution position sensors and position control. Here, absolute error results from compliance in the system, largely structural, which can be reduced in subsequent iterations. Moreover, we note that exact one-to-one motion between the input and output is not critical, as device operators are largely determining end-effector positions using visual information (e.g. the MRI scans) and tactile cues, rather than relying on proprioception. Moreover, the path following experiment indicates that with line-of-site feedback, a teleoperator of the device is able to control a tool to sub-millimeter precision and performs as well as when manipulating the output directly. This is well within the range of needle targeting accuracy reported by MRI compatible biopsy robots which fall between 1.2mm-2.55mm [6], [12], [13].

In addition to providing force transparency, system backdrivability enables reflection of respiratory motions (as well as other small movements) with minimal body wall force. Needle position remains aligned with the organ, and physicians can instruct breath-hold techniques as needed with patients inside the bore. Figure 11 illustrates that for typical breathing motions, only 5 N of force is induced. This force is largely generated by the weight of the device as it moves above the neutral position determined by the spring counterbalance. A more sophisticated mechanism with a constant counterbalance force could create a floating effect and further reduce the body wall force.

The tubing diameter was selected based on a trade-offs among viscous losses, minimum bend radius, and available fittings. Specifically, damping increases with decreasing tube diameter and is particularly affected by constrictions occurring between the piston chambers and subsequent transmission lines. For such reductions, losses grow with the ratio of diameters to the fourth power [37]. In practice, piston diameter is determined by available rolling-diaphragm dimensions. Independent of this constraint, piston diameter is limited by internal line pressure which grows with reduction in diameter to the power of two. Halving piston diameter requires a 4x increase in line pressure to maintain a given joint torque. While viscous losses increase with smaller diameters, tubing flexibility (resistance to motion from bending) decreases. Small levels of viscous friction are well tolerated by operators and for certain tasks can even improve accuracy [38]. In particular, for biopsy, manipulation occurs at relatively low velocities, minimizing impact of viscous losses. To reduce resistance from tube bending, we favor smaller diameter tubing. A standard size, 1/4 inch (6.4mm) OD, benefits from readily available plastic fittings with no metal components.

Arm joints are limited to $\pm 35^\circ$ of motion. This constraint results from the opposed piston actuator design. The piston associated with a given diaphragm consumes 1.5x the total stroke angle such that in the neutral position, the piston protrudes by half the stroke. An additional half stroke must be available in the chamber when the piston is at the neutral position. In total, each diaphragm consumes 2x its range of motion. A single rotary diaphragm can produce nearly 180°; however, when two are placed symmetrically to form a pair, the maximum becomes 90°. This produces a practical limit near 70° as some of the available 360° is needed for wall thickness separating the two chambers and a mount to the pistons. An alternative design with opposing pistons shifted to enable overlap can provide increased range of motion. Such a configuration, however, produces a net torque on the joint axes. Staggering additional pistons can to eliminate the torque (e.g. an actuator with three total pistons, two opposing one), however, this significantly increases actuator dimensions.

## VI. Summary and Conclusion

We present an MRI compatible teleoperator that passively extends physicians' reach inside the MRI bore. The approach is motivated by an initial user study with five radiologists using the final, needle insertion subsystem in combination with MRI imaging to puncture a membrane. Results showed that the interventionists required fewer MRI scans and were more accurate in detecting the instant of puncture with force reflection. We then presented a 6-axis force reflecting arm that positions the needle subsystem within the bore. We performed benchtop testing to validate the system's force transparency and backdrivability. The system passively reflects respiratory motions and enables propagation of sub-Newton forces. Operators using the device could control end-effector paths as accurately when manipulating the input of the teleoperation system as when guiding the output directly. Device passivity and backdrivability provide inherent safety and significantly lower regulation barriers. The system represents a new approach to the in-bore MRI-guided biopsy challenge.

Future work includes adding functionality to dynamically lock specific joints and scale motions. Ability to lock desired degrees of freedom (e.g. by closing valves in the fluid lines) can be used to isolate specific joints or hold the device at a fixed position. Motion scaling offers potential to improve operator precision, however, special considerations are necessary to address the inherent reciprocal coupling between motion and force. System reliability can be further improved with two point failure on each joint, as required by the FDA for this type of device. This can be achieved with duplicate lines per joint or a clutch mechanism linked to a respective joint's line pressure. In early experiments with a pig carcass, it was noted that residue on the needle (e.g. blood) occasionally resulted in slip of the collet clutch. Accordingly, future versions will explore improved materials for the collet and ability to modulate the grip force.

## Acknowledgment

The authors would like to thank Kevin Epperson, Karla Epperson, and Gary Glover for their assistance at the Stanford Lucas Center for Imaging, and in particular for facilitating on-site research activities even during COVID-19. The authors also thank Ali Kight and Ileana Pirozzi for their assistance during the user study and Hojung Choi for his assistance in device transport between facilities.

## REFERENCES


[1] M. Moche, S. Heinig, N. Garnov, J. Fuchs, T.-O. Petersen, D. Seider, P. Brandmaier, T. Kahn, and H. Busse, "Navigated mri-guided liver biopsies in a closed-bore scanner: experience in 52 patients," *European radiology*, vol. 26, no. 8, pp. 2462–2470, 2016.

[2] C. J. Das, A. H. Goenka, and D. N. Srivastava, "Mr-guided abdominal biopsy using a 1.5-tesla closed system: a feasibility study," *Abdominal imaging*, vol. 35, no. 2, pp. 218–223, 2010.

[3] R. D. Ings, "Hybrid hydrostatic rotary actuator apparatus," US Patent App. 16/298,694 Patent, Sep. 12, 2019.

[4] S. Frishman, A. Kight, I. Pirozzi, M. C. Coffey, B. L. Daniel, and M. R. Cutkosky, "Enabling in-bore mri-guided biopsies with force feedback," *IEEE transactions on haptics*, vol. 13, no. 1, pp. 159–166, 2020.

[5] H. Elhawary, Z. T. H. Tse, A. Hamed, M. Rea, B. L. Davies, and M. U. Lamperth, "The case for mr-compatible robotics: a review of the state of the art," *The international journal of medical robotics and computer assisted surgery*, vol. 4, no. 2, pp. 105–113, 2008.

[6] D. Stoianovici, C. Kim, D. Petrisor, C. Jun, S. Lim, M. W. Ball, A. Ross, K. J. Macura, and M. E. Allaf, "Mr safe robot, fda clearance, safety and feasibility of prostate biopsy clinical trial," *IEEE/ASME Transactions on Mechatronics*, vol. 22, no. 1, pp. 115–126, 2016.

[7] J. C. Vilanova, A. P. de Tudela, J. Puig, M. Hoogenboom, J. Barceló, M. Planas, S. Sala, and S. Thió-Henestrosa, "Robotic-assisted transrectal mri-guided biopsy. technical feasibility and role in the current diagnosis of prostate cancer: an initial single-center experience," *Abdominal Radiology*, vol. 45, no. 12, pp. 4150–4159, 2020.

[8] N. A. Patel, G. Li, W. Shang, M. Wartenberg, T. Heffter, E. C. Burdette, I. Iordachita, J. Tokuda, N. Hata, C. M. Tempany *et al.*, "System integration and preliminary clinical evaluation of a robotic system for mri-guided transperineal prostate biopsy," *Journal of medical robotics research*, vol. 4, no. 02, p. 1950001, 2019.

[9] D. Yakar, M. G. Schouten, D. G. Bosboom, J. O. Barentsz, T. W. Scheenen, and J. J. Fütterer, "Feasibility of a pneumatically actuated mr-compatible robot for transrectal prostate biopsy guidance," *Radiology*, vol. 260, no. 1, pp. 241–247, 2011.

[10] M. R. Van den Bosch, M. R. Moman, M. Van Vulpen, J. J. Battermann, E. Duiveman, L. J. van Schelven, H. de Leeuw, J. J. Lagendijk, and M. A. Moerland, "Mri-guided robotic system for transperineal prostate interventions: proof of principle," *Physics in Medicine & Biology*, vol. 55, no. 5, p. N133, 2010.

[11] S. Elayaperumal, M. R. Cutkosky, P. Renaud, and B. L. Daniel, "A passive parallel master–slave mechanism for magnetic resonance imaging-guided interventions," *Journal of medical devices*, vol. 9, no. 1, 2015.

[12] V. Groenhuis, F. J. Siepel, J. Veltman, J. K. van Zandwijk, and S. Stramigioli, "Stormram 4: an mr safe robotic system for breast biopsy," *Annals of biomedical engineering*, vol. 46, no. 10, pp. 1686–1696, 2018.

[13] E. Franco, D. Brujic, M. Rea, W. M. Gedroyc, and M. Ristic, "Needle-guiding robot for laser ablation of liver tumors under mri guidance," *IEEE/ASME Transactions on Mechatronics*, vol. 21, no. 2, pp. 931–944, 2015.

[14] P. Moreira, G. van de Steeg, T. Krabben, J. Zandman, E. E. Hekman, F. van der Heijden, R. Borra, and S. Misra, "The miriam robot: A novel robotic system for mr-guided needle insertion in the prostate," *Journal of medical robotics research*, vol. 2, no. 04, p. 1750006, 2017.

[15] H. Su, W. Shang, G. Cole, G. Li, K. Harrington, A. Camilo, J. Tokuda, C. M. Tempany, N. Hata, and G. S. Fischer, "Piezoelectrically actuated robotic system for mri-guided prostate percutaneous therapy," *IEEE/ASME Transactions on Mechatronics*, vol. 20, no. 4, pp. 1920–1932, 2014.

[16] W. Meinhold, D. E. Martinez, J. Oshinski, A.-P. Hu, and J. Ueda, "A direct drive parallel plane piezoelectric needle positioning robot for mri guided intraspinal injection," *IEEE Transactions on Biomedical Engineering*, vol. 68, no. 3, pp. 807–814, 2020.

[17] O. Gerovich, P. Marayong, and A. M. Okamura, "The effect of visual and haptic feedback on computer-assisted needle insertion," *Computer Aided Surgery*, vol. 9, no. 6, pp. 243–249, 2004.

[18] C. Véronneau, J. Denis, L.-P. Lebel, M. Denninger, V. Blanchard, A. Girard, and J.-S. Plante, "Multifunctional remotely actuated 3-dof supernumerary robotic arm based on magnetorheological clutches and hydrostatic transmission lines," *IEEE Robotics and Automation Letters*, vol. 5, no. 2, pp. 2546–2553, 2020.

[19] J. P. Whitney, T. Chen, J. Mars, and J. K. Hodgins, "A hybrid hydrostatic transmission and human-safe haptic telepresence robot," in *2016 IEEE international conference on robotics and automation (ICRA)*. IEEE, 2016, pp. 690–695.

[20] E. Schwarm, K. M. Gravesmill, and J. P. Whitney, "A floating-piston hydrostatic linear actuator and remote-direct-drive 2-dof gripper," in *2019 international conference on robotics and automation (ICRA)*. IEEE, 2019, pp. 7562–7568.

[21] S. Mikaiel, J. Simonelli, X. Li, Y.-H. Lee, Y. S. Lee, K. Sung, D. S. Lu, T.-C. Tsao, and H. H. Wu, "Mri-guided targeted needle placement during motion using hydrostatic actuators," *The International Journal of Medical Robotics and Computer Assisted Surgery*, vol. 16, no. 2, p. e2041, 2020.

[22] E. Mendoza and J. P. Whitney, "A testbed for haptic and magnetic resonance imaging-guided percutaneous needle biopsy," *IEEE Robotics and Automation Letters*, vol. 4, no. 4, pp. 3177–3183, 2019.

[23] K.-H. Lee, K. C. D. Fu, Z. Guo, Z. Dong, M. C. Leong, C.-L. Cheung, A. P.-W. Lee, W. Luk, and K.-W. Kwok, "Mr safe robotic manipulator for mri-guided intracardiac catheterization," *IEEE/ASME Transactions on Mechatronics*, vol. 23, no. 2, pp. 586–595, 2018.

[24] Z. Guo, Z. Dong, K.-H. Lee, C. L. Cheung, H.-C. Fu, J. D. Ho, H. He, W.-S. Poon, D. T.-M. Chan, and K.-W. Kwok, "Compact design of a hydraulic driving robot for intraoperative mri-guided bilateral stereotactic neurosurgery," *IEEE Robotics and Automation Letters*, vol. 3, no. 3, pp. 2515–2522, 2018.

[25] N. Burkhard, S. Frishman, A. Gruebele, J. P. Whitney, R. Goldman, B. Daniel, and M. Cutkosky, "A rolling-diaphragm hydrostatic transmission for remote mr-guided needle insertion," in *2017 IEEE international conference on robotics and automation (ICRA)*. IEEE, 2017, pp. 1148–1153.

[26] S. Hashemi, S. Sobojinski, and W. K. Durfee, "Low-friction antagonist hydraulic transmission using long-stroke rolling diaphragm cylinders," in *Fluid Power Systems Technology*, vol. 58332. American Society of Mechanical Engineers, 2017, p. V001T01A073.

[27] A. Gruebele, S. Frishman, and M. R. Cutkosky, "Long-stroke rolling diaphragm actuators for haptic display of forces in teleoperation," *IEEE Robotics and Automation Letters*, vol. 4, no. 2, pp. 1478–1484, 2019.

[28] M. Abayazid, C. Pacchierotti, P. Moreira, R. Alterovitz, D. Prattichizzo, and S. Misra, "Experimental evaluation of co-manipulated ultrasound-guided flexible needle steering," *The International Journal of Medical Robotics and Computer Assisted Surgery*, vol. 12, no. 2, pp. 219–230, 2016.

[29] L. Meli, C. Pacchierotti, and D. Prattichizzo, "Experimental evaluation of magnified haptic feedback for robot-assisted needle insertion and palpation," *The International Journal of Medical Robotics and Computer Assisted Surgery*, vol. 13, no. 4, p. e1809, 2017.

[30] T. Penzkofer, N. Peykan, K. Schmidt, G. Krombach, and C. K. Kuhl, "How mri compatible is "mri compatible"? a systematic comparison of artifacts caused by biopsy needles at 3.0 and 1.5 t," *Cardiovascular and interventional radiology*, vol. 36, no. 6, pp. 1646–1657, 2013.

[31] S. Okamoto, Y. Matsui, T. Hiraki, T. Iguchi, T. Komaki, T. Yamauchi, M. Uka, K. Tomita, J. Sakurai, H. Gobara *et al.*, "Needle artifact characteristics and insertion accuracy using a 1.2 t open mri scanner: A phantom study," *Diagnostic and Interventional Imaging*, 2021.

[32] S. H. Choi, S. Y. Kim, S. H. Park, K. W. Kim, J. Y. Lee, S. S. Lee, and M.-G. Lee, "Diagnostic performance of ct, gadoxetate disodium-enhanced mri, and pet/ct for the diagnosis of colorectal liver metastasis: Systematic review and meta-analysis," *Journal of Magnetic Resonance Imaging*, vol. 47, no. 5, pp. 1237–1250, 2018.

[33] P. I. Corke, "A simple and systematic approach to assigning denavit–hartenberg parameters," *IEEE transactions on robotics*, vol. 23, no. 3, pp. 590–594, 2007.

[34] S. P. Buerger, "Stable, high-force, low-impedance robotic actuators for human-interactive machines," Ph.D. dissertation, Massachusetts Institute of Technology, 2005.

[35] G. Ganesh, R. Gassert, E. Burdet, and H. Bleuler, "Dynamics and control of an mri compatible master-slave system with hydrostatic transmission," in *IEEE International Conference on Robotics and Automation, 2004. Proceedings. ICRA'04. 2004*, vol. 2. IEEE, 2004, pp. 1288–1294.

[36] T. L. Brooks, "Telerobotic response requirements," in *1990 IEEE international conference on systems, man, and cybernetics conference proceedings*. IEEE, 1990, pp. 113–120.

[37] C. C. E. Division, *Flow of fluids through valves, fittings, and pipe*. Crane Company, 1957, no. 410.

[38] V. Hayward and K. E. MacLean, "Do it yourself haptics: part i," *IEEE Robotics & Automation Magazine*, vol. 14, no. 4, pp. 88–104, 2007.

**Samuel Frishman** is a PhD candidate in the mechanical engineering department at Stanford University. He received his MS degree in mechanical engineering at Stanford University in 2017 and his BS degree in mechanical engineering at Johns Hopkins University in 2015. His research interests include medical devices, soft robotics, and haptics. He is a student member of the IEEE.

**Robert D. Ings** is co-founder of Mirsee Robotics Inc. He is experienced in designing, building and demonstrating new cost-effective technologies. At Mirsee, he leads research and development of robotic avatars and subcomponents. Mr. Ings is also co-founder and Lead Designer for a US based technology company that manufactures and distributes ARM based system-on-modules. These modules are incorporated into OEM-based products found in the aerospace, medical, military, commercial and consumer markets.

**Vipul Sheth** is an Assistant Professor in the Department of Radiology. He became interested in translational research as an undergraduate studying biomedical engineering at Case Western Reserve University. He subsequently earned his MD and PhD as part of the Case Western Reserve University Medical Scientist Training program. During his PhD dissertation he investigated measurement of pH in tumor models using a MRI contrast mechanism known as Paramagnetic Chemical Exchange Saturation Transfer (PARACEST). During radiology residency at the University of California at San Diego, he investigated new applications of the ultrashort echo time MRI technique in the brain for the evaluation of myelin in patients with cystic fibrosis. He subsequently completed a fellow ship in Body MRI at Stanford before joining the faculty in 2019.

**Bruce L. Daniel** MD received his M.D. from Harvard Medical School and is currently Professor of Radiology at Stanford University. He is a Fellow of the Society of Computed Body Tomography and Magnetic Resonance, Distinguished Investigator of the Academy of Radiology Research, and a Fellow of the American Institute for Medical and Biological Engineering. His research interest include new MRI methods, MRI-guided interventions for body and breast applications. Recently he started and now co-directs IMMERS, the incubator for medical mixed and extended reality at Stanford, a multidisciplinary collaborative hub and lab developing augmented reality visualization technology and applications that advance patient care and understanding

**Mark R. Cutkosky** received the Ph.D. degree in mechanical engineering from Carnegie Mellon University, Pittsburgh, PA, USA, in 1985. He is the Fletcher Jones Professor in mechanical engineering at Stanford University, Stanford, CA, USA. His research interests include bioinspired robots, haptics and rapid prototyping processes. Dr. Cutkosky is a Fellow of the ASME and IEEE.